Met. Mater. Int., Vol. 23, No. 5 (2017), pp. 855~864
doi: 10.1007/s12540-017-6704-y

Assessment of the Microstructure Evolution of an Austempered Ductile Iron During Austempering Process Through Strain Hardening Analysis

Riccardo Donnini[1], Alberto Fabrizi[2], Franco Bonollo[2], Franco Zanardi[3], and Giuliano Angella[1,*]

[1]Institute of Condensed Matter Chemistry and Technologies for Energy (ICMATE), National Research Council of Italy (CNR), Milan 20125, Italy
[2]Department of Engineering and Management, University of Padua, Vicenza 36100, Italy
[3]R&D Department, Zanardi Fonderie S.p.A., Minerbe 37046, Italy

(received date: 6 October 2016 / accepted date: 17 January 2017)

The aim of this investigation was to determine a procedure based on tensile testing to assess the critical range of austempering times for having the best ausferrite produced through austempering. The austempered ductile iron (ADI) 1050 was quenched at different times during austempering and the quenched samples were tested in tension. The dislocation-density-related constitutive equation proposed by Estrin for materials having high density of geometrical obstacles to dislocation motion, was used to model the flow curves of the tensile tested samples. On the basis of strain hardening theory, the equation parameters were related to the microstructure of the quenched samples and were used to assess the ADI microstructure evolution during austempering. The microstructure evolution was also analysed through conventional optical microscopy, electron back-scattered diffraction technique and transmission electron microscopy. The microstructure observations resulted to be consistent with the assessment based on tensile testing, so the dislocation-density-related constitutive equation was found to be a powerful tool to characterise the evolution of the solid state transformations of austempering.

Keywords: austempering, alloys, microstructure, ductility, tensile test

1. INTRODUCTION

Plastic behaviour of metallic alloys comes from glide resistance of mobile dislocations and strain hardening that is the raise of glide resistance because of dislocation density increase with straining. Both glide resistance and strain hardening are sensitive to the microstructure of metallic alloys, and strain hardening analysis has been often used to give indications on the microstructure evolution during the industrial processes of metallic alloys that are characterized by solid state transformations. Austempered ductile irons (ADIs) [1] are nodular ductile irons produced through proper alloying and heat-treatments, and their outstanding mechanical properties are due to the ausferrite [2-10]. During austempering, the alloys are first austenitized in the range of temperatures 850-890 °C and then isothermally held in salt bath at temperatures typically between 250 and 400 °C for the austempering transformation [9-15].

$$\gamma \rightarrow \alpha + \gamma_{HC} \quad (1)$$

Depending on the chemical composition and process temperatures, ausferrite consists of high volume fraction (up to ~ 70%) of body-centered cubic (BCC) α ferrite with residual metastable face-centred cubic (FCC) γ_{HC} austenite with high carbon content, resulting in an optimal compromise between ductility and strength [9,16,17]. Actually, α ferrite is in the form of Widmanstätten acicular laths with hardness of about HB 600, whilst γ_{HC} austenite is softer with about HB 270 [18]. Transmission Electron Microscopy (TEM) investigations [19,20] have revealed that no significant precipitation occurs in ADIs, and the high strength of this materials is due to strain hardening because of very high increase of dislocation density in ferrite α during deformation, whilst austenite γ_{HC} is strengthened by solution hardening mechanism supported by grain refinement because of twinning. However, for longer austempering times, the metastable γ_{HC} decomposes according to

$$\gamma_{HC} \rightarrow \alpha + \varepsilon' \quad (2)$$

where ε' is a metastable carbide Fe-C that causes embrittlement of ADIs [12,13].

During austempering the microstructure evolution passes through different stages [9-15]. In the early stage, individual Widmanstätten laths of α ferrite that are separated from each other by thin layers of carbon-saturated austenite γ_{HC}, nucleate at austenite grain boundaries and grow into the grain interiors. If the alloy is quenched from the austempering temperature at

*Corresponding author: giuliano.angella@cnr.it

this stage, a significant fraction of martensite is formed additionally to $\alpha + \gamma_{HC}$ structure. As the reaction proceeds, the carbon diffusion ahead of the ferritic laths becomes more difficult and the growth of the ferritic laths ceases, resulting in full $\alpha + \gamma_{HC}$ ausferrite. For longer times, the γ_{HC} fraction does not change significantly, but the deleterious precipitation of ε' carbides can take place. So the mechanical properties through tensile tests of an ADI quenched at different evolution stages of austempering should give indications of the microstructure evolution during austempering, determining hopefully the aforesaid critical range of times for the best ausferrite. In industrial production the "process window" is the range of austempering times for which the austempering reaction is finished and the precipitation of ε' carbides does not take place. In these conditions the ausferrite satisfies the requirements for the optimal compromise of mechanical properties, so the determination of this critical interval of austempering times has economical relevance in ADI production.

Constitutive equations and strain hardening analysis have been used to characterize the products of different austempering processes [9,12,13]. In these investigations the strain hardening analysis was carried out by fitting with empirical equations, like Hollomon and Hollomon-type equations, the experimental flow curves σ vs. ε_p (σ the true stress and ε_p the true plastic strain) and correlating the equation parameters with the process conditions or chemical compositions. Hollomon equation ($\sigma = K \cdot \varepsilon_p^n$) is indeed the most used constitutive equation, even if the (Hollomon-type) Ludwik equation ($\sigma = \sigma_o + K \cdot \varepsilon_p^n$) should be preferred for multiphase metallic alloys like ADIs [21-24]. In both equations, the parameters K and n are called strength coefficient and strain hardening exponent, respectively, and depend on materials and deformation conditions, as pre-strain, strain rate and temperature. However the correlations between the Hollomon parameters with microstructure have been reported to be not reliable in ductile irons, and in fact, there is no physical rationalization for the parameters K and n [21,25]. Furthermore, the application of the Hollomon equation is based on the analysis of the experimental data Log(σ) vs. Log(ε_p), whilst for Ludwik on Log($d\sigma/d\varepsilon_p$) vs. Log(ε_p) (also called Crussard-Jaoul approach): in both cases the analyses are based on the plastic strain ε_p that is an ill-defined parameter [21,25], since it depends on the mechanical history of the material.

Other constitutive equations have instead physical meaning, like the dislocation-density-related constitutive equations, among which the Voce equation is the most known [21]. The characteristic parameters of these equations can be correlated to the microstructure of materials [25], and so they should be more powerful to follow the materials evolution during solid state transformations. Furthermore, the application of these equations is based on the analysis of the experimental data trend $d\sigma/d\varepsilon_p$ vs. σ, that has been reported to be in good approximation independent on the thermo-mechanical history of materials [21].

In the dislocation-density-related constitutive equations the flow stress σ is related to the dislocation density ρ [26,27] and the increase of ρ with straining is described by the mechanistic equations of strain hardening proposed by Kocks-Mecking [28-30] and Estrin [31-33]. The parameters of these equations are intrinsically related to the microstructure of metallic materials (details of the theory are reported in Appendix I). In the case of high density of geometrical obstacles to dislocation motion, the dislocation-density-related constitutive equation [33,34] is

$$\sigma = [\sigma_S^2 + (\sigma_o^2 - \sigma_S^2) \cdot \exp(-\varepsilon_p/\varepsilon_C)]^{1/2} \quad (3)$$

here called Estrin equation. σ_s is the saturation stress corresponding to $d\sigma/d\varepsilon_p = 0$, ε_c the characteristic strain that defines the rate by which σ_s is achieved, and σ_o is the back-extrapolated stress to $\varepsilon_p = 0$. The parameters σ_s, σ_o and ε_c have physical meaning (see Appendix I), as

$$\sigma_S = M\alpha_o Gb\sqrt{\frac{1}{b\lambda r}} \text{ and } \varepsilon_C = 1/(Mr) \quad (4)$$

M is the Taylor factor (≈ 3.1 both for FCC and BCC metals, if there is no crystallographic texture [32]), α_o the dislocation-dislocation interaction strength (≈ 0.5 [32]), $G = G(T)$ is the shear modulus and b is the length of the Burgers vector. $r = r(\dot{\varepsilon}, T)$ is the function that describes the dynamic recovery depending on strain rate and temperature [30,31] and λ is the mean free path of mobile dislocations. On statistical bases λ is the average spacing between the geometrical obstacles to the mobile dislocations, so the higher the density of geometrical obstacles, the shorter λ. Geometrical obstacles to dislocation motion in ADI quenched samples are phase boundaries, like interfaces of martensite/α, α/γ_{HC} and ε' carbides. So λ can be correlated to the material microstructure, and the more complex and dense of interfaces the microstructure, the shorter λ is.

The present investigation aimed to determine a procedure based on tensile testing in order to find the critical range of austempering times for the best ausferrite. Estrin equation (Eq. 3) was fitted to the flow curves of an ADI 1050 quenched at different austempering times, and the parameters λ found through the fittings were plotted versus the austempering time. Then λ was used to characterize the alloy microstructure evolution during austempering to determine the critical range of austempering times for the best ausferrite. The microstructures of the ADI quenched samples were also analysed through conventional optical microscopy, electron back-scattered diffraction (EBSD) technique and transmission electron microscopy (TEM) in order to validate the correlation of λ with the alloy microstructure.

2. EXPERIMENTAL PROCEDURE

2.1. Mechanical characterization

An ADI 1050 with chemical composition complying to

ASTM A897/A 897M-06 [1] and nodular graphite fraction of 10 ± 1% was first austenitized, then held in a salt bath at the austempering temperature and quenched at fourteen different increasing times (t_1, t_2,..., t_{14}). Tensile tests at room temperature and strain rate 10^{-4} s^{-1} were performed on round specimens with initial gauge diameter d_o of 12.5 mm and gauge length l_o of 50.0 mm complying to ASTM E8-8M. Engineering tensile flow curves S vs. e were obtained, where $S = F/A_o$ and $e = (l - l_o)/l_o$ are the engineering stress and strain, respectively, whilst F and l are the instantaneous load and gauge length, respectively. True stress σ vs. true strain ε curves were considered, where $\sigma = S\cdot(1 + e)$ and $\varepsilon = \ln(1 + e)$. For the strain hardening analysis, the plastic component of flow curves was analysed, through considering only the plastic strain $\varepsilon_p = \varepsilon - \varepsilon_e$, with $\varepsilon_e = \sigma/E$ the elastic strain (E the experimental Young modulus). Equation 3 was fitted to the true plastic flow curves before the Considére's criterion, if achieved, that is $d\sigma/d\varepsilon_p = \sigma$, which is equivalent to the ultimate tensile strength (UTS) condition $dS = 0$. Beyond this condition, necking occurs and the flow curves are not representative of materials behavior [25].

The procedure to find the parameters from fitting Eq. 3 to the true plastic flow curves is based on the analysis of the experimental strain hardening data. In fact, (see Appendix I) , the differential form of Eq. 3 is

$$\frac{d\sigma^2}{d\varepsilon_p} = \frac{\sigma_S^2}{\varepsilon_C} - \frac{\sigma^2}{\varepsilon_C} \tag{5}$$

with

$$\frac{\sigma_S^2}{\varepsilon_C} = \Theta_S = \frac{M^3(\alpha_o G)^2 b}{\lambda} \tag{6}$$

Θ_s and $1/\varepsilon_c$ are constant during straining, so Eq. 5 states a linear relationship between ($d\sigma^2/d\varepsilon_p$) and (σ^2), where Θ_s is the intercept and $1/\varepsilon_c$ the slope of the best linear fit, respectively. In Fig. 1 an example of the procedure on a typical curve of ADI 1050 is reported. The range of experimental data ($d\sigma^2/d\varepsilon_p$) vs. (σ^2) to be fitted with Eq. 5 was not arbitrary (Fig. 1(b)), since Eq. 5 could be fitted only to a linear data region at high stresses. After having found Θ_s and $1/\varepsilon_c$ from the best linear fit of Eq. 5, σ_o could be finally worked out by fitting Eq. 3 to the experimental flow curve (Fig. 1(b)). In Fig. 1(b) Estrin equation fails at low stresses, because soon after yielding dislocations multiple profusely, evolving from transitional dislocation configurations to the dynamic equilibrium structure, when Eq. 5 holds [35]. However, it is important to underline that the aim of the present fittings was not to approximate the widest portion of flow curves, but to calculate the parameter λ that can be related to the ADI microstructure during austempering.

2.2. Microstructural characterization

Conventional optical microscopy (OM), scanning electron microscopy (SEM) with electron back-scattered diffraction (EBSD) technique and transmission electron microscopy (TEM) observations were performed to investigate the microstructure evolution of the ADI 1050 during austempering to validate the trend of the parameter λ resulting from fitting the flow curves with Estrin equation. Samples for OM investigations were first mechanically polished and then chemically etched with a 2% Nital solution for the general microstructure. In order to reveal the different phases, Beraha's reagent was used to tint differently the phases, so the OM micrographs were then processed with an image analysis software to quantify the volume fraction of α ferrite phase that appeared darker than austenite and martensite phases. The alloys microstructures were observed through a high resolution SEM SU-70 by Hitachi with an accelerating voltage of 20 kV, whilst EBSD maps were acquired through a SEM FEG-SEM, Quanta 250 FEI™ with an accelerating voltage of 20 kV. Austenite quantification and distribution of grain size were determined by means of EBSD technique carried out on 9 selected austem-

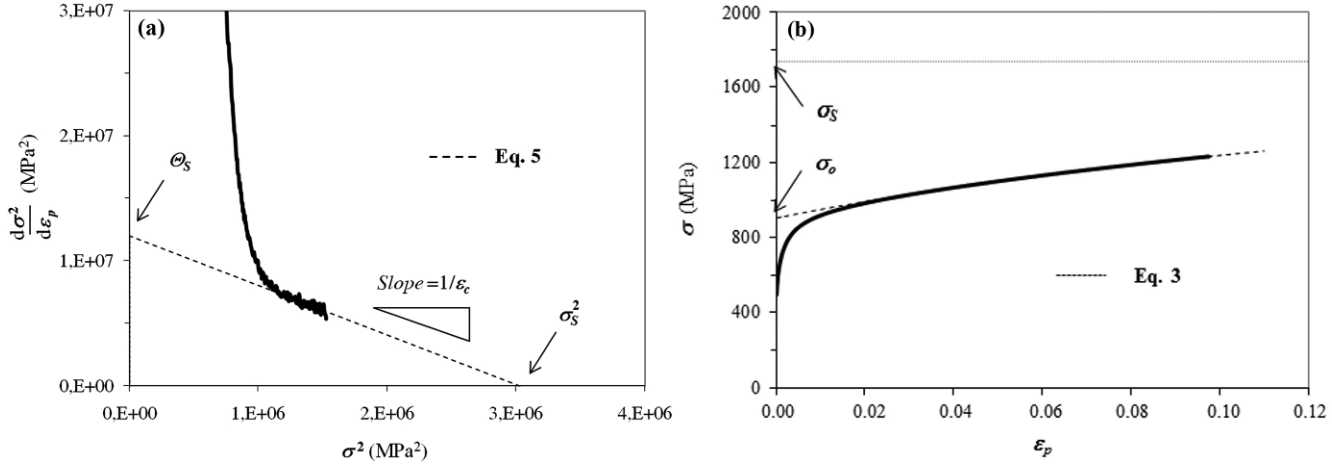

Fig. 1. (a) Determination of the constitutive equation parameters through fitting Eq. 5 to the linear region of the differential data ($d\sigma^2/d\varepsilon$) vs. (σ^2); (b) corresponding flow curve and Eq. 3 with σ_o = 907.1 MPa and σ_s = 1736.7 MPa.

pering conditions, by analyzing an area of ~ 350 × 300 μm² and a step size of 0.5 μm. The raw data were then post-processed with TSL OIM™ software. The surfaces for EBSD measurements were carefully prepared by standard mechanical polishing with diamond paste and 0.04 μm silica suspension for at least 10 minutes. Finally, TEM observations were performed on ADI 1050 after prolonged austempering times by means of the electron microscope JEOL™ 2000 EX II operating at 200 kV. The specimen for TEM was mechanically ground to a thickness of approximately 50 μm followed by ion milling at low incident angle with Precision ion polishing system 691 by Gatan™.

3. RESULTS

3.1. Strain hardening analysis

In Fig. 2 the engineering tensile flow curves S vs. e of ADI 1050 samples quenched at different increasing times (t_1, t_2, ..., t_{14}) during austempering are reported. The shapes of the flow curves changed significantly with increasing austempering time. Particularly during the early stages, the austempering transformation was not completely finished and some martensite could be produced through quenching. Until t_3 the flow curves had smooth transitions from the elastic regime to the plastic one, whilst beyond t_3 the elastic-plastic transition was sharp and the plastic flow curves were quite flat with almost linear strain hardening rates $d\sigma/d\varepsilon_p$.

In Fig. 3 ultimate tensile strength (UTS) and elongation to rupture (e_R) vs. austempering time are reported. The trends of UTS and e_R vs. austempering time were consistent to the expected microstructure evolution, since lower UTS and larger elongations to rupture were found at intermediate times, when no martensite and no ε' carbides should have been present, and the material was more ductile. Unfortunately, because of the significant irregular trends, from UTS and e_R data there was no clear indication of a precise range of times for the optimal

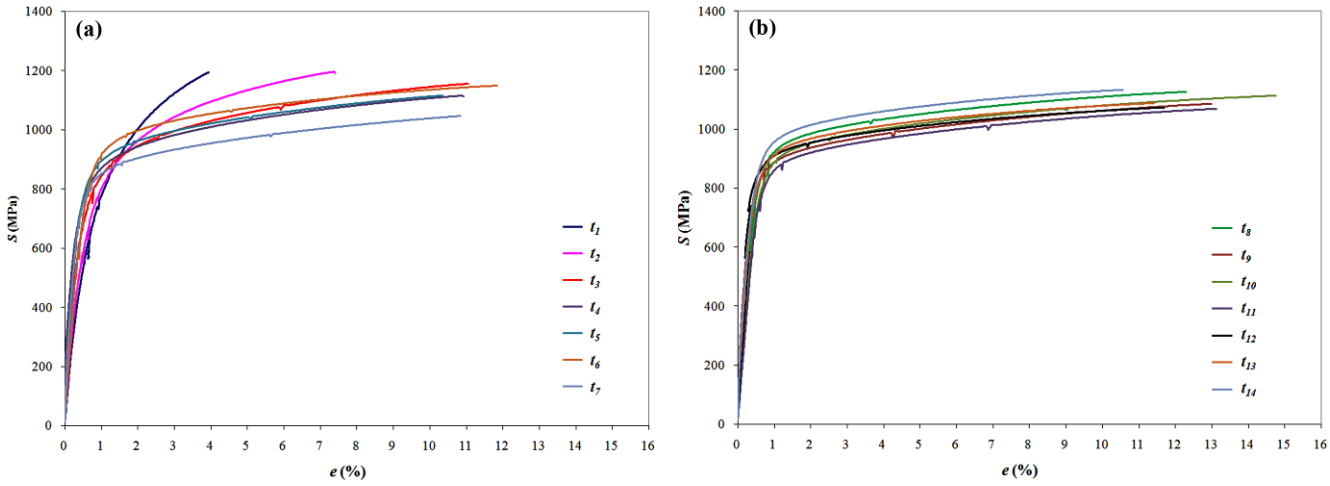

Fig. 2. Engineering flow curves of ADI 1050 quenched samples after different austempering times (arbitrary units). (a) austempering times between t_1 and t_7; (b) austempering times between t_8 and t_{14}.

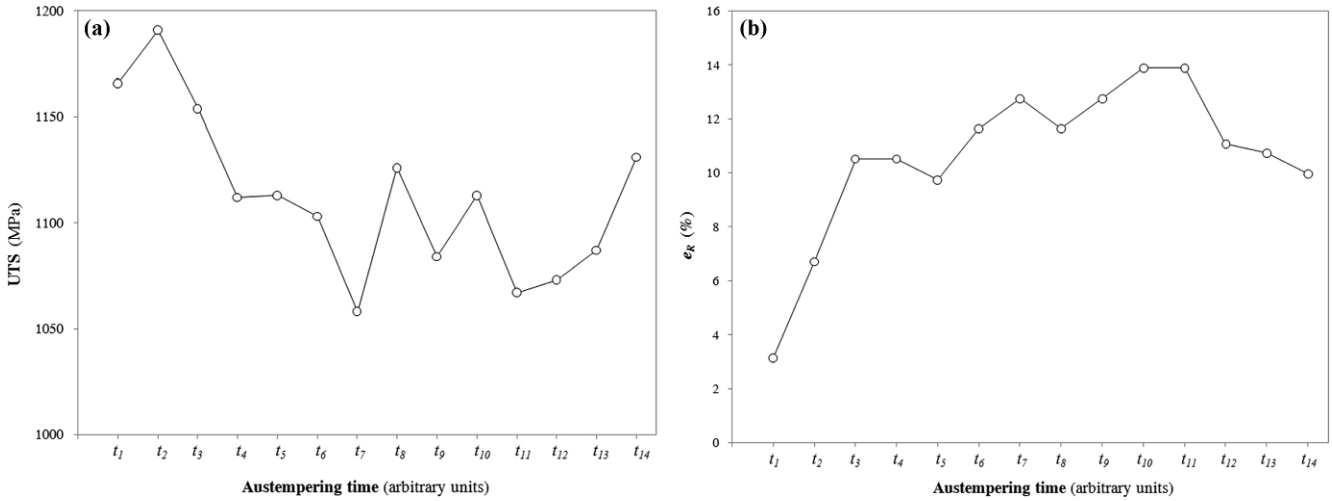

Fig. 3. (a) Ultimate tensile strength UTS vs. austempering time: ordinate axis was restricted to highlight the data scattering; (b) elongation to rupture e_R vs. austempering time.

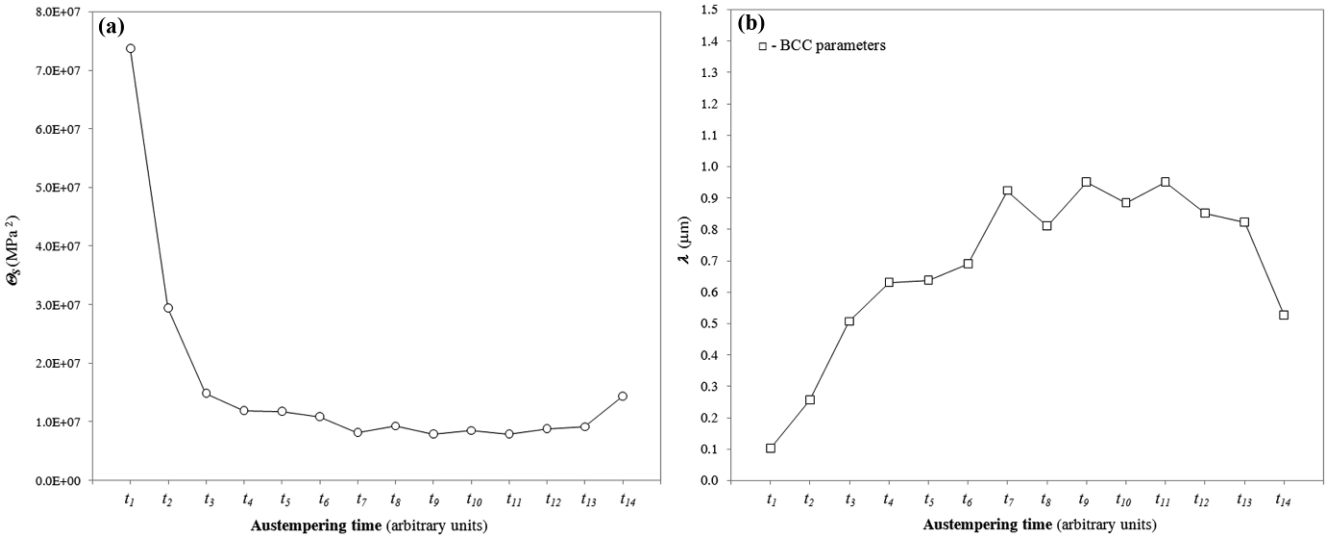

Fig. 4. Characteristic parameters of Eqs. 5 and 6: (a) dislocation multiplication term Θ_s vs. austempering time; (b) parameter λ calculated through Eq. 6 by using the BCC parameters vs. austempering time.

ausferrite.

The flow curves of ADI 1050 quenched after different austempering times were investigated through Estrin equation, and the parameters of Eq. 3 were found through the strain hardening analysis reported in Fig. 1. In Fig. 4 the parameters Θ_s and λ (Eqs. 5 and 6) against the austempering time are shown: the percentage errors associated to Θ_s and λ were about 1-7%, so no error bars were reported in the plots, since they had dimensions similar to the data symbols. In Fig. 4(a) the parameter Θ_s decreased initially and increased slightly with longer austempering times, showing a wide minimum between t_7 and t_{11}. In Fig. 4(b) the λ calculated through the BCC parameters is reported, since ferrite α represented almost 60% of the volume fraction of ADI (see Fig. 7), so $M = 3.1$, α_o

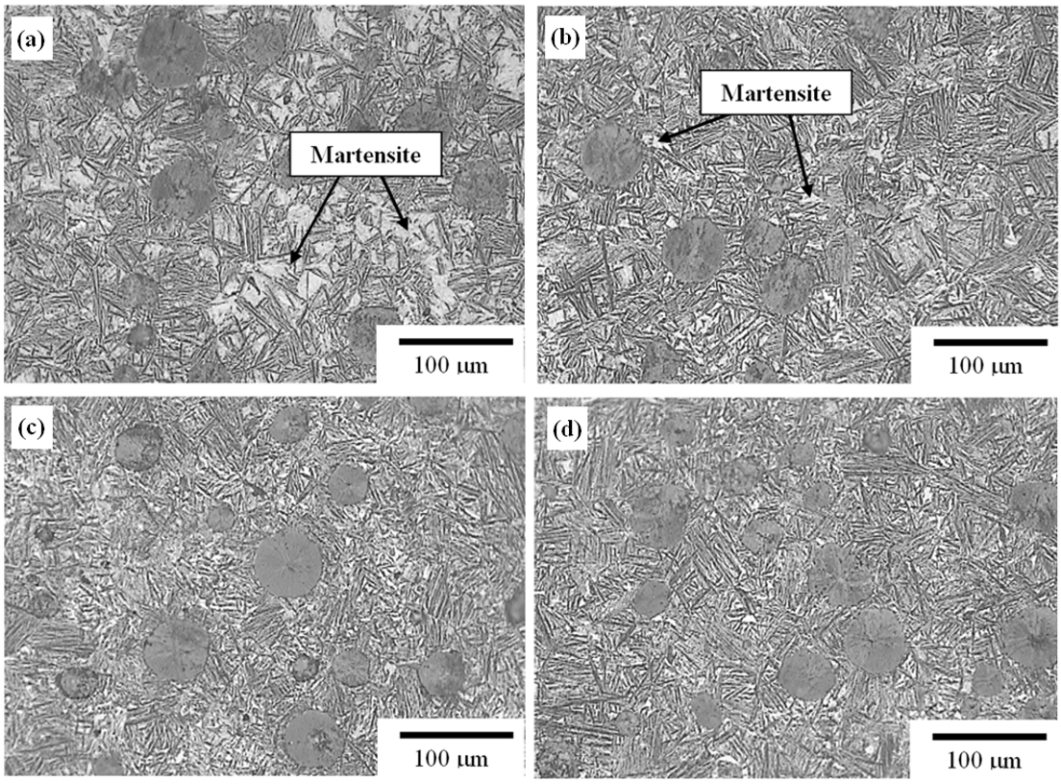

Fig. 5. Significant ADI 1050 microstructures through OM after increasing austempering times: (a) $t = t_1$; (b) $t = t_3$; (c) $t = t_7$; and (d) $t = t_{14}$.

= 0.5, G = 64 GPa and b = 0.248 nm [36] were considered in Eq. 6. The trend of the parameter λ identified clearly a range at the austempering times between t_7 and t_{11} that could be related to specific microstructure of the quenched ADI 1050 during the austempering transformation.

3.2. Microstructure analysis

Microstructure observations were gathered to verify the correlation between the parameter λ and the actual microstructure of the quenched ADI during austempering. In Fig. 5, OM micrographs of the quenched samples after selected increasing austempering times are reported. At t_1 graphite nodules and acicular structure could be detected, suggesting that some ausferrite was already formed (Fig. 5(a)). However, numerous light regions of martensite produced during quenching were visible, indicating that a significant part of austenite was not transformed yet. In Fig. 5(b) after t_3 the volume fraction of martensite was significantly reduced, so the transformation was significantly evolved. In Fig. 5(c) at t_7 no martensite could be found, demonstrating that the transformation should have been already finished, whilst in Fig. 5(d) after t_{14} there was no significant difference in the microstructure with respect to t_7.

In Fig. 6, representative EBSD phase maps of ADI 1050 quenched after different austempering times are reported. The austenite γ_{HC} (red areas) increased significantly with increasing austempering times, whilst the ferrite α + martensite volume fraction (green areas) decreased. In fact, martensite is a body-centered tetragonal phase with the c/a lattice parameter ratio that varies with the carbon content and is typically near 1, so this made no possible to distinguish martensite from BCC ferrite by using EBSD Kikuchi patterns. On the contrary,

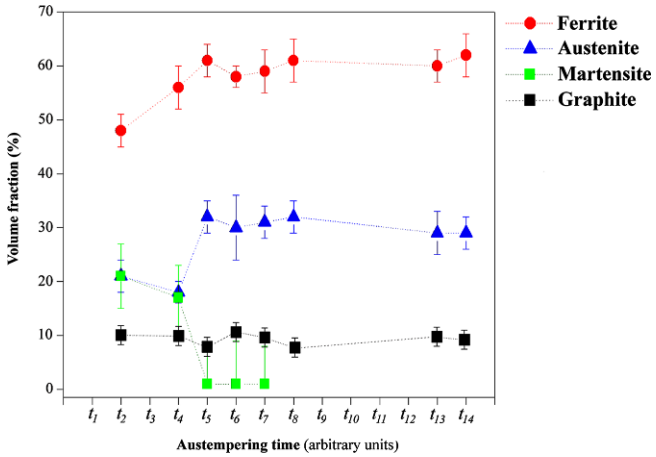

Fig. 7. Volume fractions of α, γ_{HC}, martensite and graphite as function of austempering time.

FCC austenite was easily recognized through EBSD technique. The ferrite volume fraction was estimated through digital quantitative analysis of OM micrographs after Beraha's chemical etching that tinted differently ferrite. Consequently the martensite volume fraction was determined by difference between the α + martensite volume fraction found through EBSD and the α fraction found through OM. The volume fractions of α, γ_{HC}, martensite and graphite vs. austempering time are reported in Fig. 7. In Fig. 7, the α ferrite fraction increased significantly during austempering until t_5, whilst the austenite content raised suddenly when the martensite disappeared almost completely at t_5. Beyond t_5 no appreciable variation of the microstructure was found, which suggested that the austempering reaction ended at t_5. No clear indication of increase of

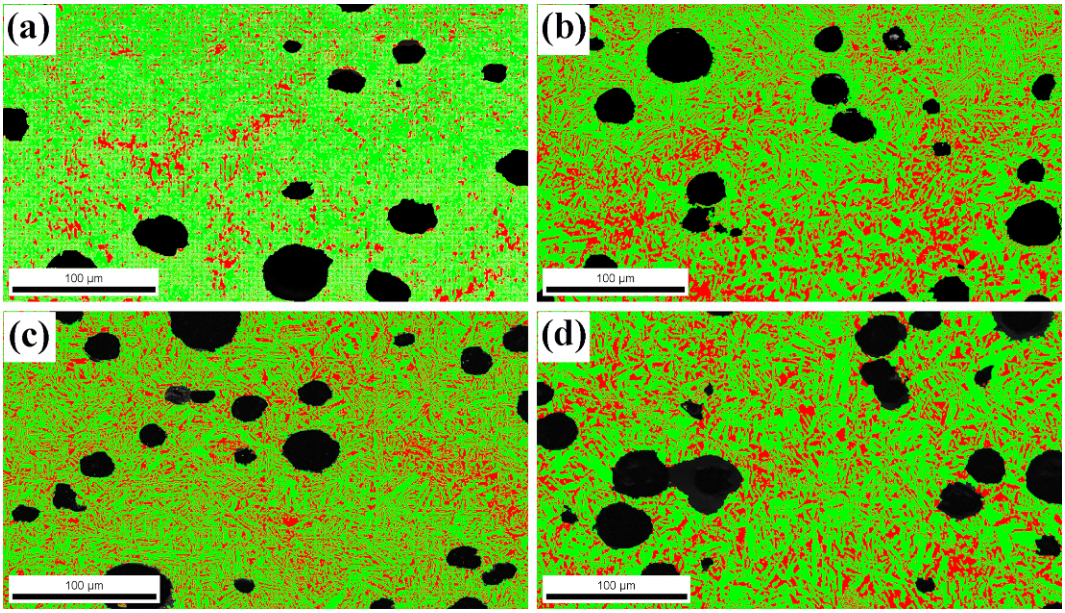

Fig. 6. EBSD phase maps of ADI 1050 microstructure after different austempering times: (a) t_2, (b) t_6, (c) t_8, and (d) t_{13}; austenite in red, ferrite + martensite in green and no-indexed points in black corresponding to nodular graphite.

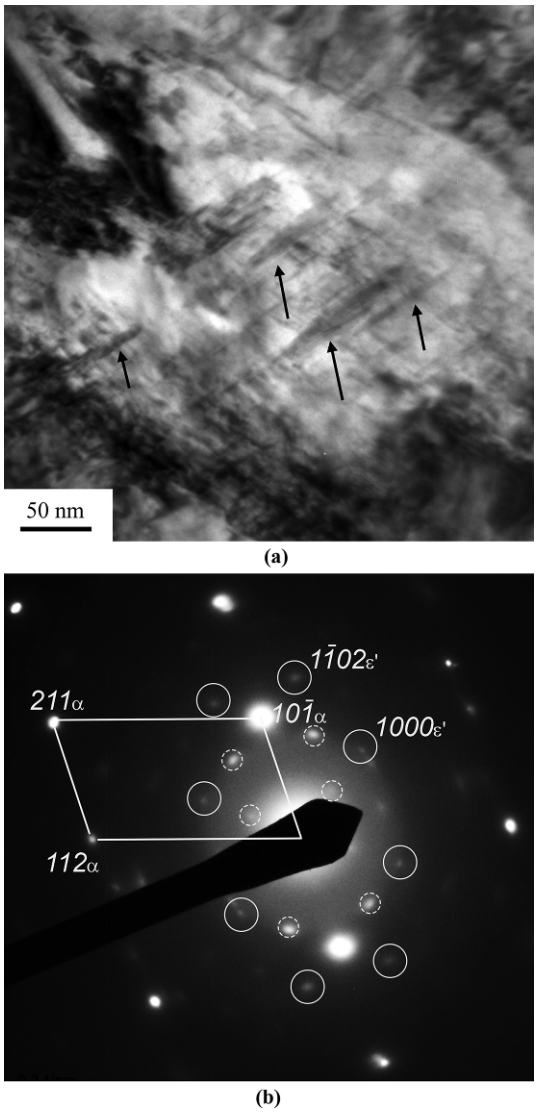

Fig. 8. TEM micrographs of ADI 1050: (a) microstructure at the austempering time t_{14}, the arrows indicate fine needle-like precipitates; (b) selected area diffraction pattern (SAED) from the microstructure in (a), with diffraction spots from ferrite α and extra spots from Fe-C ε' carbides indicated in circles (in dash circles double diffraction spots).

ferrite with decrease of austenite was found in Fig. 7 for austempering times longer than t_5, which could indicate the decomposition of austenite into ferrite and Fe-C ε' carbides.

In order to verify the stability of the ADI microstructure for longer austempering times, TEM observations were carried out on the ADI quenched samples during the last stages of the austempering reaction (Fig. 8). At t_{14} fine needle-like precipitates were found (see Fig. 8(a)) and the selected area electron diffraction (SAED) pattern corresponding to the micrograph in Fig. 8(a) is reported in Fig. 8(b). The diffraction pattern consisted of the superposition of an intense pattern and additional pale diffraction spots coming from the precipitates in Fig. 8(a). The indexing revealed that the matrix was α ferrite and the precipitates were Fe-C ε' carbides with hexagonal structure, space group $P6_322$, with lattice parameters $a = 0.2752$ nm, $c = 0.4353$ nm [37]. Additional spots were attributed to double reflections, as indicated in Fig. 8(b).

4. DISCUSSION

Plastic behaviour of metallic materials is sensitive to microstructure, so the analysis of flow curves of tensile tested quenched samples was used to have indications on the microstructure evolution of ADI 1050 during austempering. In Fig. 3 broad minimum for UTS and maximum for e_R at intermediate austempering times were consistent to an increase of volume fraction of γ_{HC} austenite, which reduced the strength of ADI 1050 and conferred higher ductility, consistently with the best ausferrite found through microstructure observations. Unfortunately, the wide scattering of the engineering parameters UTS and e_R against the austempering time could not give any precise hint about a specific critical time range for the best ausferrite.

Therefore, the analysis of the plastic behaviour was carried out through fitting the flow curves of the quenched samples with Estrin equation (Eq. 3). In Fig. 4 the parameter Θ_s found with the differential form of Estrin equation (Eq. 5) and the parameter λ (Eq. 6) showed smooth trends with wide minimum and maximum between t_7 and t_{11}, respectively. The parameter λ in Fig. 4(b) was an average of the mean free paths of mobile dislocations in the overall ADI quenched structures. In Fig. 9 a weighted average mean free path $\overline{\lambda}$ between ferrite α and austenite γ_{HC} vs. austempering time was calculated for austempering times longer than t_5 through the volume fractions of α and γ_{HC} measured with OM and EBSD techniques (Fig. 7), that was 0.60 for ferrite α and 0.30 for austenite γ_{HC}

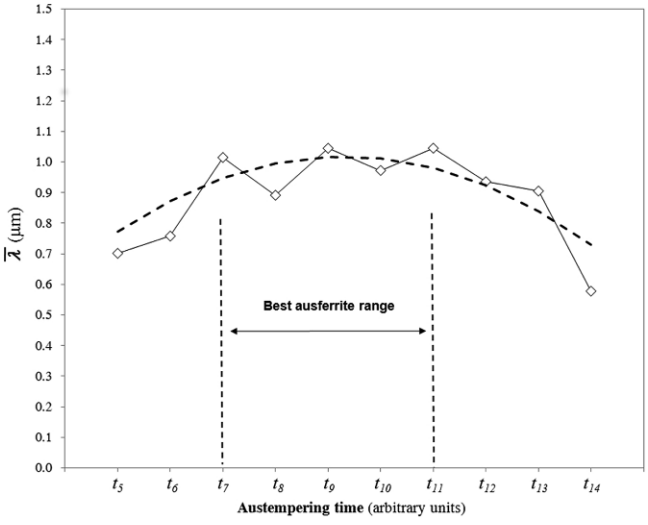

Fig. 9. The weighted average mean free path $\overline{\lambda}$ between ferrite α and austenite γ_{HC} vs. austempering time for times longer than t_5.

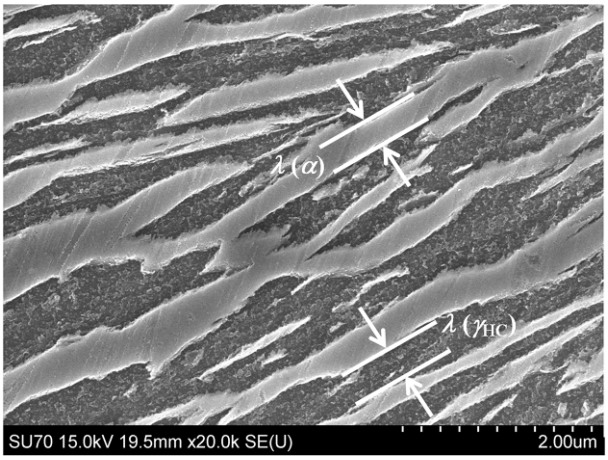

Fig. 10. SEM micrograph with secondary electrons of ADI 1050 at 20 kX: ferrite (bright areas) and austenite (dark areas).

(graphite volume fraction 0.1), whilst the volume fraction of martensite was negligible. Though the values of $\overline{\lambda}$ increased slightly with respect to λ calculated with BCC parameters in Fig. 4(b), however the trend of $\overline{\lambda}$ was unchanged with a wide maximum of about 1.0 μm between the austempering times t_7 and t_{11}, suggesting that the ADI microstructure could be stable in this range of times. In Fig. 10 the ADI 1050 microstructure at t_9 observed through SEM is reported. The microstructure consisted of $\alpha + \gamma_{HC}$ ausferrite, and it is significant to note that the widths of the lamellae α and γ_{HC} $\lambda(\alpha)$ and $\lambda(\gamma_{HC})$, respectively) varied from 0.2 to over 1.0 μm, which was consistent with the parameter $\overline{\lambda}$ found between t_7 and t_{11} in Fig. 9, supporting significantly the use of Estrin equation in describing the plastic behaviour of ADI 1050.

The microstructure results gathered with OM and EBSD techniques seemed to indicate that beyond t_5 the austempering reaction was mostly concluded. In fact for austempering times shorter than t_5 a significant volume fraction of martensite was found in the quenched ADI samples, as reported in Figs. 5-7. Beyond t_5 the volume fractions of ferrite α and austenite γ_{HC} appeared quite constant (Fig. 7), whilst the presence of martensite was almost zero. So OM and EBSD results could not give indication of eventual precipitation of Fe-C ε' carbides in the quenched samples at longer austempering times, though a reduction in ductility was indeed highlighted in Figs. 2-3. However, TEM observations (Fig. 8) revealed the precipitations of islands of ferrite α and fine needle-like precipitates in γ_{HC} austenite [38]. The corresponding selected area electron diffraction (SAED) pattern reported in Fig. 8(b) revealed the ferrite structure and additional spots that were consistent with the hexagonal structure of Fe-C ε' carbides [37], which confirmed that the deleterious decomposition of γ_{HC} into $\alpha + \varepsilon'$ occurred for longer austempering times, in agreement with the ductility reduction found in Fig. 3(b).

So, only after OM, EBSD and TEM observations, the trend of the parameters $\overline{\lambda}$ during the whole austempering from t_1 to

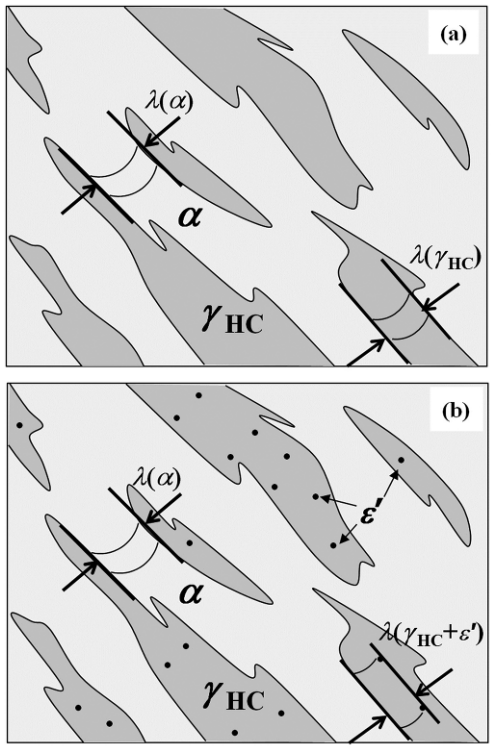

Fig. 11. Sketch of the increase of geometrical obstacles in the analyzed microstructures: (a) optimal ausferrite characterized by mean free paths $\lambda(\alpha)$ and $\lambda(\gamma_{HC})$; (b) after Fe-C ε' precipitation in γ_{HC}, the mean free path $\lambda(\gamma_{HC} + \varepsilon')$ is shorter than $\lambda(\gamma_{HC})$ because of increase of geometrical obstacles.

t_{14} in Fig. 9 could be rationalised in terms of microstructure evolution of the quenched ADI 1050 samples. According to the theory of strain hardening [28-33], $\overline{\lambda}$ is inversely proportional to the density of geometrical obstacles in the material, in this case the interfaces of martensite/α, α/γ_{HC} and also the interfaces between Fe-C ε' precipitates and $\alpha + \gamma_{HC}$ matrix. All these microstructural features hindered the dislocation motion. Therefore, at austempering times shorter than t_7 a complex microstructure consisting of three phases, i.e. ferrite, austenite and some martensite, was present, with a high density of geometrical obstacles and, thus, shorter $\overline{\lambda}$. With increasing austempering times (longer than t_7), the austempering transformation was exhausted with no presence of martensite (Figs. 5-7), and stable ausferrite with lower density of interfaces and larger $\overline{\lambda}$ of about 1.0 μm consistent to SEM observations (see Fig. 10) was achieved. However, after austempering times longer than t_{11}, the precipitation of Fe-C ε' carbides (TEM micrographs in Fig. 8) leaded to a consequent increase of geometrical obstacles density in the overall microstructure and decrease of $\overline{\lambda}$. In Fig. 11 a simplified sketch reports that $\lambda(\gamma_{HC} + \varepsilon')$ became shorter than the original $\lambda(\gamma_{HC})$ of the best ausferrite because of Fe-C ε' precipitation. Though $\lambda(\alpha)$ remained unchanged, Fe-C ε' precipitation resulted in the reduction of the weighted average mean free path $\overline{\lambda}$. In conclusion, at

intermediate austempering times (between t_7 and t_{11}) the parameter $\overline{\lambda}$ achieved a maximum because of proper ausferrite with no martensite and no Fe-C ε' carbides. Therefore the trend of the parameter $\overline{\lambda}$, found from modelling the plastic behaviour of ADI 1050 with Estrin equation, and the microstructure observations converged to identify the critical range of austempering times for the best ausferrite between the austempering times t_7 and t_{11}.

5. CONCLUSION

The aim of this investigation was to determine a procedure based on tensile testing to find the critical range of austempering times to obtain the best ausferrite having the optimal compromise of mechanical properties. An ADI 1050 was quenched after different increasing austempering times, and the quenched samples were deformed in tension. Estrin equation that is a dislocation-density-related constitutive equation, was used to fit the plastic flow curves of the ADI 1050 samples quenched at different austempering times, and the parameters of this equation were correlated to the microstructures of the alloy during austempering. The samples microstructures were also analysed through conventional optical microscopy, electron back-scattered diffraction (EBSD) technique and transmission electron microscopy (TEM) to validate this correlation. From the procedure based on Estrin equation a weighted average mean free path $\overline{\lambda}$ related to the microstructure of the quenched ADI 1050 during austempering could be found. The dislocation-density-related constitutive equation used to model flow curves of materials with high density of geometrical obstacles to dislocation motion (Estrin equation) revealed a very good correlation between the equation parameters and the microstructure evolution during austempering of ADI 1050. The procedure based on tensile testing and Estrin equation can be considered a powerful tool to assess the evolution of the solid state transformations of industrial processes of metallic alloys.

ACKNOWLEDGEMENT

Mr. E. Veneri, F. Vettore and S. Masaggia from R&D Laboratory Zanardi Fonderie S.p.A. are warmly thanked for their technical support.

APPENDIX I

In FCC and BCC metals with geometrical obstacles to dislocation motion, the flow stress is given by [26,27]

$$\sigma = \sigma_f + \sigma_{Or} + M\alpha_o Gb\rho^{1/2} \quad \text{(I1)}$$

σ_f is the friction stress because of solid solution and Peierls-Nabarro stress (the latter negligible in FCC metals), whilst σ_{Or} is the stress to overcome geometrical obstacles through bowing according to the Orowan mechanism. The third term is related to dislocation-dislocation interactions and depends on the total dislocation density ρ. M is the Taylor factor, α_o the dislocation-dislocation interaction strength, $G = G(T)$ is the shear modulus and b is the length of the Burgers vector. According to the mechanistic equation of strain hardening proposed by Kocks-Mecking [28-30] and developed by Estrin [31-33], if the density of geometric obstacles to dislocation motion is much larger than that of the obstacles caused by dislocation structures [31], the increase of ρ because of plastic strain ε_p (strain hardening) is given by [30-33]

$$\frac{d\rho}{d\varepsilon_p} = M\cdot\left(\frac{1}{b\lambda} - r\cdot\rho\right) \quad \text{(I2)}$$

M and b have the usual meaning and λ is the mean free path of mobile dislocations. On statistical bases λ is the average spacing between the geometrical obstacles to the mobile dislocations. $r = r(\dot{\varepsilon}, T)$ is the function that describes the dynamic recovery depending on strain rate and temperature [30,31]. Equation I2 states that strain hardening consists of two competing mechanisms: the first positive term in the right member of Eq. I2 (inversely proportional to λ) is the hardening because of dislocation multiplication and storage; the second negative term is the softening because of annihilation of dislocations with opposite Burgers vectors, and formation of low energy dislocation structures, which are called dynamic recovery as whole.

According to [31] for a simplified approach, a direct effect of the geometrical obstacles and lattice friction to the flow stress can be disregarded, so $\sigma \approx M\alpha_o Gb\rho^{1/2}$, and substituting $\rho = (\sigma/M\alpha_o Gb)^2$ in Eq. I2 results in [33,34]

$$\frac{d\sigma^2}{d\varepsilon_p} = \frac{M^3(\alpha_o G)^2 b}{\lambda} - Mr\sigma^2 \quad \text{(I3)}$$

Equation I3 can be written as

$$\frac{d\sigma^2}{d\varepsilon_p} = \frac{\sigma_S^2}{\varepsilon_C} - \frac{\sigma^2}{\varepsilon_C} \quad \text{(I4)}$$

with

$$\sigma_S^2 = \frac{(M\alpha_o G)^2 b}{\lambda r} \text{ and } \varepsilon_C = 1/(Mr) \quad \text{(I5)}$$

σ_s is the saturation stress corresponding to $d\sigma/d\varepsilon_p = 0$, ε_c the characteristic strain that defines the rate with which σ_s is achieved. Integrating Eq. I4 results in the Estrin equation

$$\sigma = [\sigma_S^2 + (\sigma_o^2 - \sigma_S^2)\cdot\exp(-\varepsilon_p/\varepsilon_C)]^{1/2} \quad \text{(I6)}$$

REFERENCES

1. ASTM A897/A 897M-06, *Standard Specification for Austempered Ductile Iron Castings*, ASTM International, West Conshohocken, PA.

2. Y. J. Kim, H. Shin, H. Park, and J. Lim, *Mater. Lett.* **62**, 357 (2008).
3. M. H. Sohi, M. N. Ahmadabadi, and A. B. Vahdat, *J. Mater. Process. Tech.* **153-154**, 203 (2004).
4. J. L. Hernández-Rivera, R. E. Campos Cambranis, and A. de la Garza, *Mater. Design* **32**, 4756 (2011).
5. S. Panneerselvam, C. J. Martis, S. K. Putatunda, and J. M. Boileau, *Mat. Sci. Eng. A* **626**, 237 (2015).
6. A. Basso, J. Sikora, and R. Martinez, *Fatigue Fract. Eng. M.* **36**, 650 (2013).
7. M. Soliman, A. Nofal, and H. Palkowski, *Mater. Des.* **87**, 450 (2015).
8. D. O. Fernandino, J. M. Massone, and R. E. Boeri, *J. Mater. Process. Tech.* **213**, 1801 (2013).
9. J. Yang and S. K. Putatunda, *Mat. Sci. Eng. A* **382**, 265 (2004).
10. F. Zanardi, F. Bonollo, N. Bonora, A. Ruggiero, and G. Angella, *Int. J. Metalcast.* **11**, 136 (2017).
11. A. Basso, R. Martínez, and J. Sikora, *J. Alloy. Compd.* **509**, 9884 (2011).
12. J. Olofsson, D. Larsson, and I. L. Svensson, *Metall. Mater. Trans. A* **42**, 3999 (2011).
13. A. Meena and M. El Mansori, *Metall. Mater. Trans. A* **43**, 4755 (2012).
14. R. E. Smallman, I. R Harris, and M. A. Duggan, *J. Mater. Process. Tech.* **63**, 18 (1997).
15. H. Fredriksson, J. Stjerndahl, and J. Tinoco, *Mat. Sci. Eng. A* **413**, 363 (2005).
16. J. Dodd, *Mod. Cast.* **68**, 60 (1978).
17. I. Schmidt and A. Schuchert, *Z. Metallkd.* **78**, 871 (1987).
18. Zanardi Fonderie SpA, *Internal report*, http://zanardifonderie.com/en/(accessed February 19, 2014).
19. M. Kaczorowski and D. Myszka, *Prace ITMat.* **SS**, 10 (2003).
20. A. Krzyńska and M. Kaczorowski, *Arch. Foundry Eng.* **7**, 111 (2007).
21. R. E. Reed-Hill, W. R. Crebb, and S. N. Monteiro, *Metall. Mater. Trans. A* **4**, 2665 (1973).
22. G. E. Dieter, *Mechanical Metallurgy*, p.286, McGraw-Hill Book Company Publisher, USA (1988).
23. H. J. Kleemola and M. A. Nieminen, *Metall. Mater. Trans. A* **5**, 1863 (1974).
24. B. K. Choudhary, E. I. Samuel, K. B. S. Rao, and S. L. Mannan, *Mater. Sci. Tech.* **17**, 223 (2001).
25. G. Angella, F. Zanardi, and R. Donnini, *J. Alloy. Compd.* **669**, 262 (2016).
26. D. Hull and D. J. Bacon, *Introduction to Dislocations*, p.197, Butterworth-Heinemann Publisher, UK (2002).
27. R. W. K. Honeycombe and H. K. D. Bhadeshia, *Steels - Microstructure and Properties*, p.13, Butterworth- Heinemann Publisher, UK (1995).
28. U. F. Kocks, *J. Eng. Mater-T. ASME* **98**, 76 (1976).
29. U. F. Kocks and H. Mecking, *Acta Metall.* **29**, 1865 (1981).
30. U. F. Kocks and H. Mecking, *Prog. Mater. Sci.* **48**, 171 (2003).
31. Y. Estrin, *Dislocation Density Related Constitutive Modelling in: Unified Constitutive Laws of Plastic Deformation* (eds. A. S. Krausz and K. Krausz), pp.66-106, Elsevier, Netherlands (1996).
32. Y. Estrin and H. Mecking, *Acta Metall.* **32**, 57 (1984).
33. Y. Estrin, *J. Mater. Process. Tech.* **80-81**, 33 (1998).
34. J. P. Sah, G. J. Richardson, and C. M. Sellars, *J. Aus. Inst. Metals* **14**, 292 (1969).
35. G. Angella, D. Donnini, D. Ripamonti, and M. Maldini, *Mat. Sci. Eng. A* **594**, 381 (2014).
36. H. J. Frost and M. F. Ashby, *Deformation-Mechanism Maps*, p. 32, Pergamon Press, UK (1982).
37. F. Y. Hung, L. H. Chen, and T. S. Lui, *Mater. Trans*. **45**, 2981 (2004).
38. J. H. Jang, I. G. Kim, and H. K. D. H. Bhadeshia, *Scripta Mater*. **63**, 121 (2010).